All-Dielectric Silicon Nanoslots for Er^{3+} Photoluminescence Enhancement

Boris Kalinic[,1,*] Tiziana Cesca[,1] Sandro Mignuzzi[,2] Andrea Jacassi[,2] Ionut Gabriel Balasa[,1]
Stefan A. Maier[,3,2] Riccardo Sapienza[,2] and Giovanni Mattei[1]

[1]*Department of Physics and Astronomy, University of Padova, Via Marzolo 8, I-35131 Padova, Italy*

[2]*The Blackett Laboratory, Department of Physics, Imperial College London, London SW7 2BW, United Kingdom*

[3]*Chair in Hybrid Nanosystems, Nanoinstitute Munich, Faculty of Physics, Ludwig-Maximilians-Universität München, Königinstrasse 10, 80539 München, Germany*

We study, both experimentally and theoretically, the modification of Er^{3+} photoluminescence properties in Si dielectric nanoslots. The ultrathin nanoslot (down to 5-nm thickness), filled with Er in SiO$_2$, boosts the electric and magnetic local density of states via coherent near-field interaction. We report an experimental 20-fold enhancement of the radiative decay rate with negligible losses. Moreover, via modifying the geometry of the all-dielectric nanoslot, the outcoupling of the emitted radiation to the far field can be strongly improved, without affecting the strong decay-rate enhancement given by the nanoslot structure. Indeed, for a periodic square array of slotted nanopillars an almost one-order-of-magnitude-higher Er^{3+} PL intensity is measured with respect to the unpatterned structures. This has a direct impact on the design of more efficient CMOS-compatible light sources operating at telecom wavelengths.

I. INTRODUCTION

Since the pioneering work of Purcell, it is well known that the radiation properties of an emitter can be controlled by its photonic environment [1]. In the weak-coupling regime, according to Fermi's Golden Rule, the radiative decay rate is proportional to the matrix element that connects the excited state with the ground state and the local density of photonic states (LDOS) [2]. In recent years, a huge effort has been directed to the quest of engineering the radiative properties of an emitter to obtain novel and increasingly efficient photonic sources. With this aim in mind, the design of the photonic environment down to the near field proves fundamental for the control of the radiative decay rate through the modification of the LDOS [3–7]. Indeed, the realization of antennas and cavities (either metallic or all-dielectric) with dimensions much smaller than the emission wavelength has attracted growing interest in the field of nanophotonics, as a path to emission engineering. The coupling of emitters with plasmonic nanostructures has been deeply investigated, showing the possibility of achieving high Purcell factors for emitters in close proximity [8–16]. Nevertheless, the occurrence of a nonradiative energy transfer toward the metallic nanostructures limits the efficiency of the amplification process, decreasing the quantum efficiency of the emitting system [17,18] and raising serious limitations for cutting-edge

applications such as quantum technologies. More recently, all-dielectric nanoantennas and nanocavities have received increasing interest due to the possibility of obtaining electric and magnetic field enhancements through Mie resonances with negligible absorption losses [19–24]. While the enhancement factor due to Mie resonance is usually limited to 1–10, recently inverse [25], mode-matching [26], and coherent [7] innovative designs of dielectric nanostructures have shown that Purcell enhancements up to 3 orders of magnitude are possible, and in a broad spectral range. Nevertheless, due to technological difficulties in the choice and the processing of the materials suitable for this purpose, the predicted decay-rate variations are still very challenging to reach experimentally [27–29].

Despite the recent progress in the enhancement of nanostructured silicon light emission [30,31], due to the indirect band gap, Si-based light sources are still extremely inefficient. Nevertheless, the distinctive optical properties of silicon in the near infrared (NIR) (i.e., a high refractive index with negligible absorption) make the material attractive in the field of nanophotonics and optoelectronics [20,32,33]. In this framework, the combination of an emitting layer made of erbium-doped silica embedded in a silicon nanostructure may represent an ideal CMOS-compatible nanocavity for light amplification at telecom wavelengths [34,35]. Indeed, Er-doped silica-based materials are of strategic interest in the field of optoelectronics due to the sharp Er^{3+} radiative emission at $\lambda = 1540$ nm, a wavelength that matches the minimum absorption window

---

*boris.kalinic@unipd.it

of silica and that is transparent for silicon [32,36]. Nevertheless, the long lifetime of the $^4I_{13/2}$ excited state (of the order of milliseconds) makes the Er^{3+} emission sensitive to nonradiative recombination and concentration-quenching processes [37,38]. Therefore, the increase of the Er^{3+} radiative decay rate is of fundamental importance for improving the luminescence efficiency and, thus, the design of novel photonic devices based on Er-doped materials, including on-chip optical amplifiers [39,40], light-emitting diodes (LEDs) [41], lasers [42,43], and single-photon sources at telecom wavelengths [28,44]. In addition to the technological importance, the mixed electric dipole (ED) and magnetic dipole (MD) transition of the Er^{3+} radiative emission makes it an interesting probe for the investigation of the selective electric and magnetic LDOS modification in dielectric nanostructures, which could open up new routes for the control of the radiative properties of quantum emitters by engeneering both ED and MD resonances [5,45].

In the present work, we investigate, both experimentally and theoretically, the modification of the Er^{3+} radiative decay rate and the photoluminescence (PL) intensity in silicon planar and pillarlike nanoslots. For the planar geometry, we report an approximately 20-fold enhancement of the Er^{3+} radiative decay rate on a 5-nm-thick Er-doped silica film between two silicon layers. Almost perfect agreement is observed between the experimental

findings and the classical dipole-oscillator (CDO) model first proposed by Chance *et al.* [46], which describes the lifetime variations of an emitter in close proximity to planar interfaces. The far-field efficiency of the planar nanoslot is also calculated, pointing out that, although the probability of Er^{3+} radiative decay turns out to be more than one order of magnitude higher, most of the emitted radiation is coupled to guided modes in silicon and just a small fraction of it emerges in the far field. To this respect, we show that an increase of the Er^{3+} emission properties can be obtained via modifying the geometry of the silicon nanoslot. A periodic square array of nanopillars with the Er-doped layer sandwiched between two 200-nm-thick silicon nanodisks is nanofabricated: due to the modified slot geometry, the coupling of the emitted radiation out of the photonic structure turns out to be strongly increased, with an enhancement of about one order of magnitude of the Er^{3+} photoluminescent intensity in the far field, without significantly affecting the radiative decay-rate acceleration.

II. METHODS

A. Sample nanofabrication

The magnetron cosputtering technique is used to deposit erbium-doped silica ($Er:SiO_2$) thin films with different thicknesses ranging from 5 nm to 90 nm on silicon substrates. A sketch of the samples is shown in Fig. 1(a).
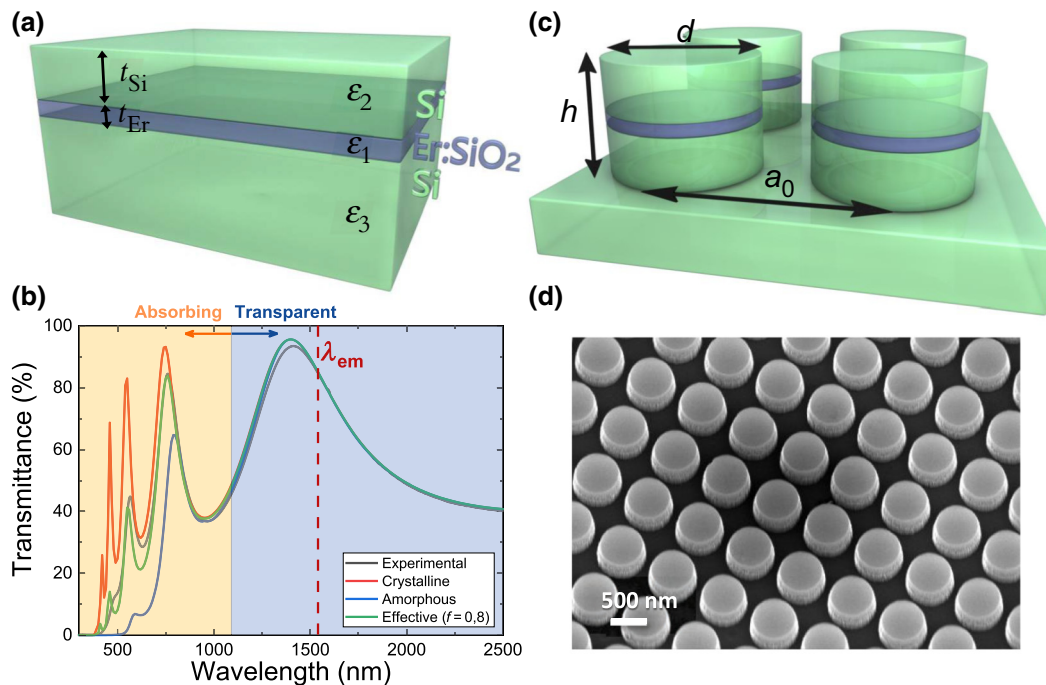

FIG. 1. Sample synthesis. (a) A sketch of the S_x_Si samples. (b) Transmittance spectra: the dark gray line indicates the experimentally measured data; red and blue curves are calculated from tabulated dielectric functions of monocrystalline and amorphous silicon, respectively; the green line indicates the transmittance spectrum calculated with an effective medium approximation, where $f = 0.8$ is the filling fraction of the monocrystalline component. (c) A sketch of the S_x_Pillar samples. (d) A 20°-tilted SEM image of the two-dimensional (2D) square array of silicon slotted nanopillars (i.e., sample S_10_Si).

A metallic erbium target (diameter 2 in., thickness 1/4 in., purity 99.99%, by K. J. Lesker) is mounted on a dc source, while a silicon-dioxide target (diameter 2 in., thickness 1/8 in., purity 99.9%, by K. J. Lesker) is placed on a radio-frequency (rf) source. The depositions are performed at a pressure of 5×10^{-3} mbar, in a slightly oxidizing atmosphere (95% Ar + 5% O_2) in order to obtain stoichiometric SiO_2 layers. Both sources are tilted by about $25°$ to head toward the center of the sample holder, which is kept under rotation to ensure the homogeneity of the deposited films. The power of the two sources is set to keep the Er concentration below the concentration-quenching limit ([Er] < 1% at.) [37,47]. Before the deposition, the silicon substrates are cleaned in a "piranha" solution (3:1—concentrated H_2SO_4: 30% H_2O_2) for 1 h and rinsed in ultrapure water. Thickness and roughness of the deposited films are determined by atomic-force-microscopy (AFM) measurements with a NT-MDT Solver-Pro AFM in noncontact mode. Rutherford backscattering spectrometry (RBS) is used to determine the Er concentration [Fig. S1(a)] and to exclude the presence of contaminants in the Er:SiO_2 layer. After the Er:SiO_2-thin-film deposition, the samples are annealed at $850°C$ for 2 h in vacuum ($P \sim 5 \times 10^{-5}$ mbar) to recover the matrix defects and to activate the Er^{3+} luminescence at $\lambda = 1540$ nm ($^4I_{13/2} \rightarrow {}^4I_{15/2}$ transition) [48].

A silicon overlayer (210 ± 10 nm thick, measured by AFM) is deposited on the top of half of each sample by magnetron sputtering. In this case, a 2 in. Si target is mounted on the dc source and the deposition is done at a power $P = 100$ W, in a pure-argon atmosphere to avoid Si oxidation during the deposition. In this way, for each Er:SiO_2 thickness, two different areas on the same sample are obtained: one with the Si overlayer and the other without (air overlayer). In the following, the samples are named according to the thickness of the Er:SiO_2 film and the overlayer material: for example, the sample S_30_Si has a 30-nm-thick Er:SiO_2 film with a Si overlayer deposited on top of it. The samples are further cleaned in a "piranha" solution and annealed at $850°C$ for 2 h in vacuum ($P \sim 5 \times 10^{-5}$ mbar) to promote silicon densification and crystallization and to recover the defects at the Si/SiO_2 interface. X-ray diffraction (XRD) measurements show that the Si films are in an amorphous phase in the as-deposited samples but they become polycrystalline after the annealing, with a grain size of about 10 nm [see Fig. S1(b)]. To characterize the transmittance properties of the deposited Si overlayer, an additional sample is prepared by sputtering the Si thin film on a transparent substrate (SiO_2 slab by Heraeus). The transmittance spectrum is measured using a JASCO V670 spectrophotometer and compared to those calculated considering monocrystalline ($\varepsilon_{c,i}$) and amorphous ($\varepsilon_{a,i}$) tabulated Si dielectric functions [49]. The experimental data can be fitted considering an effective dielectric function [50]: $\varepsilon_{\text{eff},i} = f \varepsilon_{c,i} + (1-f) \varepsilon_{a,i}$, where

$f = 0.8$ is the monocrystalline Si filling fraction [see Fig. 1(b)]. Such an effective medium is consistent with a polycrystalline silicon film, where the amorphous component of the effective dielectric function is necessary to take into account grain boundaries and defects present in the sputtered and annealed layer. After the thermal annealing at $850°C$, a reduction of about 5% of the Si-film thickness is observed, which results in $t_{\text{Si}}^{\text{ann}} = 200 \pm 10$ nm. This is due to the densification and the amorphous-to-polycrystalline phase transition of the silicon thin film during the high-temperature annealing [51].

On two selected samples with Er:SiO_2 layers of thickness 10 nm and 60 nm, respectively, with the Si overlayer, an area of 1×1 mm^2 is patterned with a square-lattice array of nanopillars by means of electron-beam lithography (EBL) and reactive ion etching (RIE) [Figs. 1(c) and 1(d)]. In the following, the two samples are named S_10_Pillar and S_60_Pillar. The deposited silicon thin film, the Er:SiO_2 layer, and the Si substrate are etched in a single RIE process (pure CF_4 atmosphere) to obtain multilayered pillars with heights $h = 410$ nm and $h = 460$ nm for the S_10_Pillar and S_60_Pillar samples, respectively. Thus, the Er-doped layer is in the middle of each pillar, with a 200-nm-thick Si layer on top and below it. The square-lattice parameter is $a_0 = 800$ nm, while the pillar diameter is $d = 660$ nm.

B. PL measurements

Time-resolved PL measurements are performed at room temperature using as the excitation source a picosecond pulsed mode-locked Nd:YAG laser (Leopard by Continuum—pulse duration 18 ps, repetition rate 10 Hz) coupled with an optical parametric amplifier (TOPAS by Light Conversion), which allows us to tune the laser wavelength in the (420–2400)-nm range. The excitation wavelength is set at $\lambda_{\text{ex}} = 520$ nm to match the $^4I_{15/2} \rightarrow {}^2H_{11/2}$ Er^{3+} absorption transition, where the Er^{3+} excitation cross section in silica is a maximum within the visible and NIR range [52]. The pulse energy is $E \sim 0.5$ mJ and the angle of incidence is $30°$ with respect to the normal to the sample surface. The PL signal is collected normally to the sample surface with a converging lens (NA = 0.26) and focused on the entrance slit of a single grating monochromator coupled to a N_2-cooled photomultiplier tube (Hamamatsu R5509-72). Time-resolved PL analyses are carried out by fixing the detected wavelength at 1540 nm and collecting the PL-intensity decay as a function of time with a digital oscilloscope (Tektronix TDS 7104). PL spectra are recorded in a confocal configuration, exciting the samples with the $\lambda = 488$ nm line of a multiline cw argon laser (i.e., in resonance with the $^4I_{15/2} \rightarrow {}^4F_{7/2}$ Er^{3+} absorption transition), mechanically chopped at 10 Hz. The incident beam is focused onto the sample through a microscope objective ($60\times$, NA = 0.85, by Newport) that is used also to

collect the emitted PL signal at 1540 nm. The incident photon flux is $\phi = 9 \times 10^{19}$ cm^{-2} s^{-1}, much lower than the PL-intensity saturation conditions for Er^{3+} in SiO$_2$ [53]. A dichroic mirror (transmittance cut-on at 650 nm) is used to separate the excitation beam from the PL signal, which is recorded by means of a single-grating monochromator with the NIR N$_2$-cooled photomultiplier tube coupled to a lock-in amplifier triggered by the chopper frequency.

C. Analytical and numerical methods

For a two-level ED emitter in a double-interface structure [see the sketch in Fig. 1(a)], the radiative decay rate, as a function of the distance from the interfaces (d_1 and d_2, with $d_1 + d_2 = t_{\text{Er}}$), can be estimated for the transverse (γ_t) and the parallel (γ_p) orientation with respect to the interfaces using the CDO model according the following equations [32,46]:

$$\frac{\gamma_t^{\text{ED}}(d_1, d_2)}{\gamma_{0,R}^{\text{ED}}} = \frac{3}{2} \text{Im} \left[\int_0^\infty \frac{F(\hat{d}_1, -r_{1,2}^p) F(\hat{d}_2, -r_{1,3}^p)}{F(\hat{d}_1 + \hat{d}_2, -r_{1,2}^p r_{1,3}^p)} \frac{u^3}{a_1} du \right],$$
(1)

$$\frac{\gamma_p^{\text{ED}}(d_1, d_2)}{\gamma_{0,R}^{\text{ED}}} = \frac{3}{4} \text{Im} \left[\int_0^\infty \left[\frac{F(\hat{d}_1, r_{1,2}^s) F(\hat{d}_2, r_{1,3}^s)}{F(\hat{d}_1 + \hat{d}_2, -r_{1,2}^s r_{1,3}^s)} \right. \right.$$
$$\left. \left. + \frac{F(\hat{d}_1, r_{1,2}^p) F(\hat{d}_2, r_{1,3}^p)}{F(\hat{d}_1 + \hat{d}_2, -r_{1,2}^p r_{1,3}^p)} (1 - u^2) \right] \frac{u}{a_1} du \right],$$
(2)

where $u = k_\parallel / k$ is the parallel normalized component of the wave vector **k**, $\gamma_{0,R}^{\text{ED}}$ is the intrinsic ED radiative decay rate, $F(x, y) = 1 + y \exp(-2a_1 x)$, and $\hat{d}_1 = 2\pi \sqrt{\varepsilon_1} d_1 / \lambda$ and $\hat{d}_2 = 2\pi \sqrt{\varepsilon_1} d_2 / \lambda$ are the normalized distances from the upper (2) and lower (3) interface, respectively. $r_{i,j}^s$ and $r_{i,j}^p$ are the two-layer Fresnel reflection coefficients for s- and p-polarized light:

$$r_{i,j}^s = \frac{a_i - a_j}{a_i + a_j}, \quad r_{i,j}^p = \frac{\varepsilon_i a_j - \varepsilon_j a_i}{\varepsilon_i a_j + \varepsilon_j a_i},$$
(3)

where $a_n = -i(\varepsilon_n / \varepsilon_1 - u^2)^{1/2}$ is the perpendicular normalized component of the wave vector **k** and ε_n is the dielectric function of the nth layer.

The nominal intensity of the Ar laser impinging on the Er:SiO$_2$ film (I_{pump}) is computed using EMUstack [54]. The simulations are performed at $\lambda = 488$ nm and at normal incidence and at 10° with respect to the surface normal (this can be considered a good approximation of our experimental conditions, since the divergence of the Ar laser beam at the sample position is estimated to be ±6°). A more comprehensive description of the EMUstack simulations is reported in the Supplemental Material

[55]. The dielectric function determined from the analysis of the transmittance spectra is used for the deposited Si layer, whereas tabulated dielectric functions are used for all the other layers [49].

III. RESULTS AND DISCUSSION

A. Radiative decay-rate enhancement

To investigate the radiative decay-rate variation in a nanostructured thin film experimentally where the emitting layer is confined in a sandwich of high-refractive-index layers, a set of samples with decreasing thicknesses of the Er:SiO$_2$ film (from 90 nm down to 5 nm) is deposited on silicon substrates. Figure 2(a) shows the evolution of the measured Er^{3+} decay rate (Γ) as a function of the Er:SiO$_2$ thickness. The experimentally acquired PL decay curves are fitted with a stretched exponential decay function and the effective decay rate is calculated as described in Ref. [53]. Nevertheless, for all the investigated samples, the stretching parameter turns out to be close to 1, indicating a low dispersion in the decay rates of the Er^{3+} ions.

For the set of samples with the Si overlayer (half-black squares), a strongly superlinear increment of the decay rate is observed when decreasing the thickness of the emitting layer. For the 5-nm-thick sample, the decay rate reaches a value of 2060 ± 80 s^{-1}, i.e., a factor of approximately 20 with respect to the Er^{3+} radiative decay rate in homogeneous silica (of about 100 s^{-1}) [4,45,56]. This behavior can be understood considering that the refractive-index contrast between the medium in which the emitters are embedded (SiO$_2$) and the two media sandwiching it substantially increases the LDOS available for the Er^{3+} emitters and this variation is stronger as the separation distance between the emitters and the interfaces is reduced [5,57]. It is worth noting that the reference samples (i.e., those with an air overlayer—gray squares) show a nonlinear increase of the decay rate as well but by decreasing the thickness of the emitting layer the effect is considerably lower (a maximum decay rate of approximately 500 s^{-1} is obtained for the S_5_Air sample).

Since the experimental decay rate always measures the sum of radiative (Γ_R) and nonradiative (Γ_{NR}) contributions, the deconvolution of the two contributions by means of an analytical model is crucial in order to determine the quantum efficiency [$q = \Gamma_R / (\Gamma_R + \Gamma_{\text{NR}})$] of the photonic system. It is worth specifying that in the following we use Γ to indicate the decay rate of a distribution of emitters, whereas γ is for a single emitter placed at a certain distance from an interface. For a two-level ED emitter, the radiative decay rate as a function of the slot thickness (t_{Er}) can be estimated according to Eqs. (1) and (2). The Er^{3+} $^4I_{13/2} \rightarrow {}^4I_{15/2}$ transition has a mixed character, with a nearly equal contribution of ED and MD components
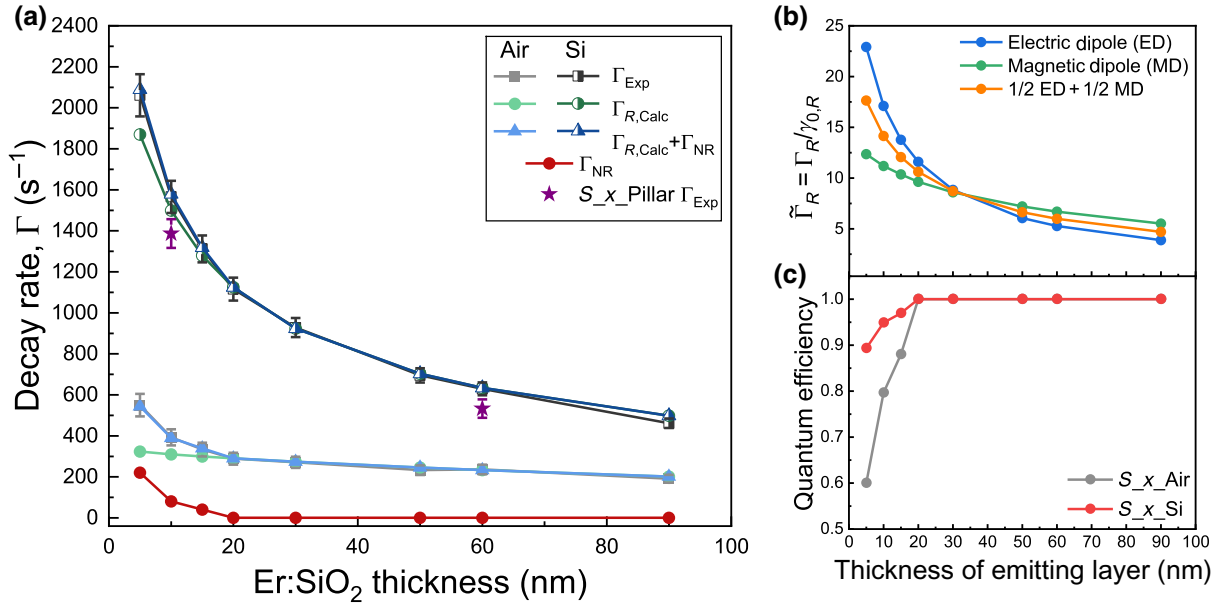
FIG. 2. (a) The decay rate (Γ) versus the Er:SiO$_2$ layer thickness. The gray and half-black squares indicate the experimentally measured decay rates for the S_x_Air and S_x_Si sets of samples, respectively. The solid and half-green dots indicate the calculated radiative decay rate, while the blue triangles are the sum of the radiative and nonradiative decay rates for the two sets of samples. The red dots show the calculated nonradiative decay rate ($\Gamma_{NR} = \Gamma_{Exp} - \Gamma_{R,Calc}$). The purple stars indicate the measured decay rate for the S_x_Pillar samples. (b) The computed normalized radiative decay rate ($\widetilde{\Gamma}_R = \Gamma_R/\gamma_{0,R}$) as a function of the emitting layer thickness for ED, MD, and mixed (i.e., 1/2ED + 1/2MD) emitters with an isotropically averaged orientation. The emitters are embedded in a silica layer that is enclosed between two semi-infinite silicon films. (c) The calculated quantum efficiency of the S_x_Si and S_x_Air set of samples.

[5,45], therefore the latter also has to be taken into account for the correct interpretation of the Er³⁺ emission process. For a MD emitter, the decay rate can be calculated with the same Eqs. (1) and (2), but interchanging $r^s_{i,j}$ with $-r^p_{i,j}$ [58,59]. Since the emitters in the active layer (Er:SiO$_2$ in our case) have no preferential orientation with respect to the interface, the isotropic configuration can the determined as $\gamma_{iso}(d_1, d_2) = \frac{1}{3}\gamma_t(d_1, d_2) + \frac{2}{3}\gamma_p(d_1, d_2)$ (where $\gamma_t(d_1, d_2)$ is for the transverse dipole—perpendicularly oriented with respect to the interface—and $\gamma_p(d_1, d_2)$ is for dipoles parallel to the interface). It is worth emphasizing that the CDO model computes the ED and MD decay-rate modification in terms of the electric and magnetic fields at the dipole position reflected from the interfaces (i.e., when the field is in phase the decay rate becomes enhanced, while when out of phase it is inhibited [59]). Moreover, since the equations are written for a single distance of the emitter from the interfaces but the experimental samples actually have a homogeneous Er³⁺ distribution in the thickness of the active layer, the approach described in Ref. [57] is followed to account for the boxlike distribution of the emitter along the sample thickness. In the Supplemental Material [55], the variation of the normalized radiative decay rate [$\gamma^{iso}(d_1, d_2)/\gamma_{0,R}$] inside the nanoslot is reported for a 60-nm-thick SiO$_2$ layer with air and a silicon overlayer.

In Fig. 2(b), the normalized radiative decay rate ($\widetilde{\Gamma}_R = \Gamma_R/\gamma_{0,R}$) of isotropically oriented ED and MD quantum emitters (at $\lambda_{em} = 1540$ nm) in SiO$_2$ ($\varepsilon^{1540}_{SiO_2} = 2.085$) placed between two semi-infinite Si films ($\varepsilon^{1540}_{Si} = 12.1$) is reported as a function of the thickness of the active layer. A Si overlayer of 200 nm can be considered optically thick in terms of the decay-rate modification, since a further increase of the thickness produces variations below 5% of the calculated decay rate [55]. The data show clearly that sandwiching the emitters between two high refractive index layers can significantly increase the normalized radiative decay rate, resulting, for a film a few nanometers thick, in an enhancement of more than one order of magnitude [33]. Moreover, it is worth emphasizing that since the imaginary part of the silicon dielectric function is negligible at $\lambda = 1540$ nm, the modification of the decay rate is due only to the variation of the LDOS [32,60] and no nonradiative decay channel is introduced in the photonic system (e.g., excitation of surface plasmon polaritons or lossy surface waves [56,61,62]). The increase of the radiative decay rate of more than one order of magnitude can be exploited to boost the luminescence efficiency of ED and MD emitters with low quantum efficiency [33]; e.g., for an emitting system with $q = 0.1$, a 20-fold enhancement of the decay rate predicted for the 5-nm-thick sample can push the quantum efficiency up

to 0.7, provided that the nonradiative decay rate (Γ_{NR}) is unchanged. Moreover, such a lifetime shortening is of great technological importance, since it can help to overcome some important limitations of slow emitters (such as rare-earth elements) [63]. Indeed, the increase of the Purcell factor in silicon nanoslots can be exploited to achieve gain and stimulated emission in these structures [32,64].

To compare the experimental findings with the CDO model, the ED and MD radiative decay rate ($\gamma_{0,R}^{ED}$ and $\gamma_{0,R}^{MD}$) for erbium in silica need to be known. To this end, we perform an additional set of time-resolved PL measurements on the reference samples, varying the refractive index of the overlayer medium on top of the emitting layer [65] (for details, see the Supplemental Material [55]) and we obtain $\gamma_{0,R}^{ED} = \gamma_{0,R}^{MD} = 53 \pm 3$ s^{-1}, in good agreement with the values found in Ref. [45]. Hence, it is possible to calculate the nonradiative decay rate in the experimental samples, which turns out to be negligible for the samples with $t_{Er} \geq 20$ nm and equal to 40, 80, and 220 s^{-1} for the samples with $t_{Er} = 15, 10,$ and 5 nm, respectively [red dots in Fig. 2(a)]. The onset of nonradiative decay channels can be attributed to distortions of the Er^{3+} octahedral structure in the SiO$_2$ matrix at the interfaces and their presence contributes to the total decay rate in a more pronounced way for the thinnest samples: indeed, the value of Γ_{NR} decreases when the thickness of the Er:SiO$_2$ film is increased and becomes negligible in the thickest samples. In Fig. 2(c), the calculated quantum efficiency (q) is reported for the set of samples with air and a Si overlayer. Due to the rise of the nonradiative decay rate, the thinner samples of the S_x_Air set present a drop in the quantum efficiency, which, indeed, decreases to 60% for the S_5_Air sample. Conversely, this effect is much less prominent for the S_x_Si samples, where q remains above 90% for the whole set, since the onset of a nonradiative-decay probability is counterbalanced by a much stronger enhancement of the Purcell factor. Nevertheless, the onset of nonradiative-decay probabilities in the thinnest sample could represent a possible limitation in terms of quantum application, where the reduction of the quantum efficiency could be detrimental for the optical coherence of the emitters. A possible way to mitigate or even suppress such a quantum-efficiency decrease can be to better decouple the emitters from the interface by, for example, introducing a thin undoped silica spacer layer between the emitting layer and the silicon surfaces. Nevertheless, further investigations are needed to prove this approach and to optimize the quantum efficiency of the emitting layer in the ultrathin nanoslot. In Fig. 2(a), the comparison between the experimentally measured and analytically computed (with the CDO model) decay rates is reported (half-black squares and half-blue triangles, respectively). An almost perfect agreement between the two sets of values is obtained, which confirms that the proposed nanoslot system can be used efficiently to enhance (by up to more than one order

of magnitude) the radiative decay rate of suitably coupled quantum emitters. It is worth emphasizing that this approach is not restricted to emitters in the NIR spectral region (such as Er^{3+} emitters) but can also be extended to the visible region, provided that a high-refractive-index contrast between the medium embedding the emitters and the two surrounding layers is realized (with a negligible imaginary part of the dielectric function in order not to quench the emitter luminescence). For example, GaP has recently attracted increasing interest due to its high refractive index (i.e., $n > 3$) and the band gap of 2.24 eV that makes it transparent in a wide spectral range in the visible [7,27].

B. PL-intensity enhancement

Besides the effect on the emission efficiency, the Si-nanoslot geometry also produces changes in the intensity of the PL emission. Figure 3(a) reports the evolution of the photoluminescence intensity, I_{PL}, at $\lambda = 1540$ nm as a function of the slot thickness for the S_x_Si set of samples. For an incident photon flux, $\Phi = I_{pump}/h\nu$, far from the saturation condition, the Er^{3+} PL intensity can be expressed as [66]

$$I_{PL} = Kq\beta\sigma_{Er}C_{Er}t_{Er}\frac{I_{pump}}{h\nu}, \qquad (4)$$

where K is the collection efficiency of the experimental setup, $h\nu$ is the pump photon energy, I_{pump} is the intensity of the pumping beam, q is the quantum efficiency, σ_{Er} is the Er^{3+} excitation cross section at $\lambda = 488$ nm, C_{Er} is the Er^{3+} concentration in silica, and t_{Er} is the thickness of the emitting layer. β is the so-called far-field efficiency, defined as $\beta = \Gamma_{FF}/\Gamma_R$, in which Γ_{FF} the probability of emission of radiation in the half-space above the sample [60,62]. Although the PL measurements are performed far from the saturation condition [53], it is interesting to note that I_{PL} does not increase linearly with the number of optically active erbium ions (i.e., the Er:SiO$_2$ thickness). Since K, C_{Er} and σ_{Er} can be assumed constant and the quantum efficiency varies just slightly for the whole S_x_Si set of samples [$q > 0.9$; see Fig. 2(c)], the nonlinear trend of I_{PL} is mainly determined by the variation of the far-field efficiency (β) and the intensity of the pumping beam impinging on the Er:SiO$_2$ layer (I_{pump}) as a function of the sample thickness.

The CDO model can be used to predict how the power emitted from the electric and magnetic dipoles is coupled in and out-of the photonic structure [60] and thus to calculate the probability that the emitted radiation will couple with modes that are radiating in the far field (Γ_{FF}). In the inset of Fig. 3(b), a plot of the dissipated power density [i.e., the integrand of Eqs. (1) and (2)] is reported as a function of the normalized in-plane wave vector ($u = k_\parallel/k$) for ED and MD emitters with an isotropic configuration and
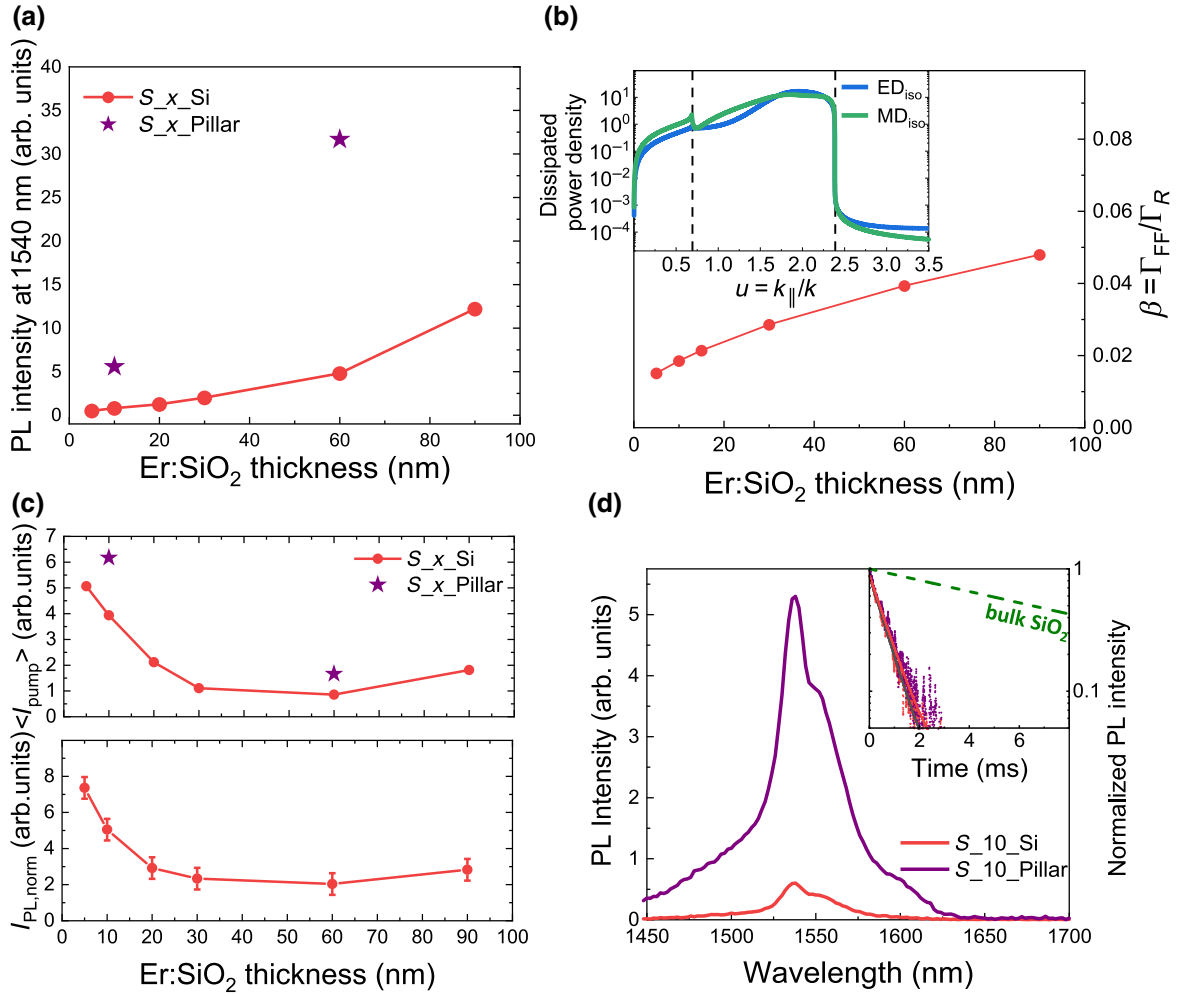
FIG. 3. PL-intensity measurements. (a) I_{PL} at 1540 nm versus the sample thickness for the S_x_Si and S_x_Pillar sets of samples. (b) The calculated far-field efficiency (β) for the S_x_Si samples. The inset shows the dissipated power density (logarithmic scale) versus the normalized in-plane wave vector, u, for ED and MD emitters in the middle of a 10-nm-thick SiO₂ film surrounded by a semi-infinite and 200-nm-thick Si layer. The vertical dashed lines indicate the critical values of u for the emitted radiation to propagate in air and in silicon. (c) The average incident power on the Er:SiO₂ layer as a function of the sample thickness (upper panel) and the normalized PL intensity, $I_{PL,norm}$ (see text), for the S_x_Si set of samples (lower panel). (d) Er³⁺ PL emission spectra in the (1450–1700)-nm-wavelength range for the S_10_Si and S_10_Pillar samples under identical excitation conditions. The inset shows the PL decay curves at $\lambda = 1540$ nm of the two samples are compared to that of Er³⁺ in SiO₂ (green dashed line).

located in the middle of a 10-nm-thick slot between a semi-infinite and a 200-nm-thick silicon layer. The two vertical dashed lines indicate the critical values of u for the emitted radiation to propagate in air and in silicon ($u = n_{Air}/n_{SiO_2}$ and $u = n_{Si}/n_{SiO_2}$, respectively). For both kinds of dipole, most of the emitted power is directed toward the silicon substrate or coupled to guided modes in the upper Si layer [32]. Indeed, integrating the dissipated power density from $u = 0$ to $u = n_{Air}/n_{SiO_2}$, it is possible to calculate the far-field decay rate (Γ_{FF}) and consequently the far-field decay efficiency ($\beta = \Gamma_{FF}/\Gamma_R$). For the whole set of S_x_Si samples, β turns out to be below 0.06 and decreases with the thickness of the Er:SiO₂ film [see Fig. 3(b)], indicating that just a small fraction of the emitted radiation

can be collected in the half-space normal to the sample surface.

Furthermore, the electric field of the incident beam inside the Er:SiO₂ film is simulated using EMUstack [54, 55]. From the computed fields at $\lambda = 488$ nm, the average pumping beam intensity, $\langle I_{pump} \rangle$, inside the Er:SiO₂ film is calculated according to Eq. (S3) in the Supplemental Material [55] and is reported in the upper panel of Fig. 3(c). The pumping intensity is modulated by the interference between the transmitted and the reflected beams inside the SiO₂ layer: the destructive interference turns out to be stronger for the 60-nm-thick silica layer and decreases considerably as the thickness of the emitting layer is decreased [see Fig. S6(a) of the Supplemental Material [55]]. The

maximum average incident intensity is obtained for the S_5_Si sample, turning out to be approximately 5 times higher than the value computed for the 60-nm-thick sample. The values of $\langle I_{\text{pump}} \rangle$ simulated with an inclination of the incident beam of $10°$ from the normal to the surface of the sample do not differ considerably from those simulated at normal incidence, indicating that the divergence of the pumping beam ($\pm 6°$) has a negligible effect on the average power inside the Er:SiO$_2$ layer. Finally, to have a better insight into the I_{PL} trend reported in Fig. 3(a), it is worth comparing the average pumping intensity at $\lambda_{\text{ex}} = 488$ nm with the PL intensity at 1540 nm normalized to the thickness of the emitting layer and to the quantum and far-field efficiencies: $I_{\text{PL,norm}} = I_{\text{PL}}/(t_{\text{Er}}\beta q)$ [upper and lower panel in Fig. 3(c), respectively]. The trend in the two plots is very similar, indicating that the nonlinear trend of the PL intensity for the S_x_Si set of samples is mainly dictated by the changes in the intensity of the incident beam caused by interference in the multilayered structure.

Since silicon has a negligible absorption at $\lambda = 1540$ nm, the fraction of the emitted power that does not emerge from the top surface is not dissipated inside the structure and could be collected, for example, from the side of the sample [64]. Nevertheless, a possible drawback of this approach could be that the polycrystalline silicon thin film may induce high propagation losses (of the order of 50 cm^{-1}) [64], thus limiting the efficiency of the collection process. A possible way to overcome the low far-field efficiency but maintain the radiative decay-rate enhancement could be to confine the emitting layer in a fully three-dimensional (3D) dielectric nanostructure [7,20,22]. In this way, the high-refractive-index contrast that drives the LDOS variation is preserved but the modified geometry can be used to redirect the emitted radiation toward the far field, limiting the propagation of the light in the silicon layers [67]. To verify this approach, two selected samples (S_10_Si and S_60_Si) are patterned with a bidimensional square array of cylindrical slotted nanopillars. The emitting layer (an Er-doped silica nanodisk) is placed in the middle of each pillar, with a 200-nm-thick Si layer on top and below it. In this way, multilayered pillars are produced with heights of $h = 410$ nm and 460 nm for the S_10_Pillar and S_60_Pillar samples, respectively [see the sketch in Fig. 1(c) and the SEM image in Fig. 1(d)]. We choose to pattern the samples with a dense array of nanostructures in order to keep the emitting surface per unit area (the Er:SiO$_2$ filling fraction in the unit cell is $\delta = 0.52$) as high as possible. In the following, the two samples are named S_10_Pillar and S_60_Pillar.

The Er^{3+} emission spectra in the (1450–1700)-nm-wavelength range for the S_10_Si and S_10_Pillar samples are shown in Fig. 3(d), while the PL time-integrated intensity for both the two nanopatterned samples is indicated with purple stars in Fig. 3(a). Despite having half of the

emitting volume ($\delta = 0.52$), the two nanopatterned samples exhibit a strong enhancement of the PL intensity at $\lambda = 1540$ nm. In both cases, an increase by a factor of approximately 7 with respect to the corresponding unpatterned samples is observed, indicating that the outcoupling of the emitted radiation is strongly increased by the bidimensional periodic patterning of the photonic structure: in this way, the radiation, which is otherwise confined inside the Si films, has an additional momentum that directs the light toward the far field (i.e., the air half-space).

The PL decay curves at $\lambda = 1540$ nm for the S_10_Pillar and S_10_Si samples are reported in the inset of Fig. 3(d) and compared to that of Er^{3+} in silica [the values of the decay rates for both of the nanopatterned samples are indicated with purple stars in Fig. 2(a)]. Similarly to the behavior observed on the silicon planar nanocavities, the S_x_Pillar samples present a strong Er^{3+} decay-rate enhancement that is inversely proportional to the Er:SiO$_2$ thickness: in particular, the 10-nm-thick sample exhibits a 15 times higher decay rate with respect to the Er^{3+} radiative decay rate in bulk silica. For both samples, the measured decay rate (Γ_{Exp}) turns out to be comparable with the values obtained for the corresponding unpatterned samples, suggesting that the designed geometry does not substantially affect the average emitter LDOS inside the nanoslot, which turns out to be mainly influenced by the nanoslot geometry. Indeed, the observed decay-rate modification can be predicted to a good approximation by the CDO model, which accounts just for a planar geometry [$\Gamma_{\text{exp}}^{\text{pillar}} \sim 0.9\Gamma_{R,\text{Calc}}$; see the purple stars versus the half-green dots in Fig. 2(a)]. Moreover, the nanopatterning of the photonic structure does not increase the probability of nonradiative decay and it turns out that the high quantum efficiency of the emitting layer is also preserved for the slotted nanopillars.

Finally, it is also worth considering how the incident electric field is distributed inside the Er:SiO$_2$ nanodisk. In the Supplemental Material [55], an example of the electric field distribution obtained from EMUstack simulations is shown for the two nanopatterned samples. In both cases, no field hot spots can be observed but the normalized average intensity is roughly double for the S_x_Pillar samples compared to the corresponding unpatterned samples [see the purple stars in Fig. 3(c)]. Therefore, the increase of the incident average intensity in the Er:SiO$_2$ layer compensates the decrease of the emitting volume but the enhancement of the PL intensity by almost one order of magnitude that is observed for the S_x_Pillar samples has to be attributed to a modification of the Er:SiO$_2$ far-field radiation pattern. A rough estimate of the far-field efficiency can be obtained from Eq. (4) by comparing the measured PL intensities of the planar and pillarlike sets of samples. For both of the S_x_Pillar samples, the fraction of the emitted power directed to the air half-space

turns out to be around 0.4. Hence, the 2D array of silicon slotted nanopillars can act as an efficient all-dielectric nanoantenna that is able to strongly accelerate and direct out of the photonic structure the light emitted by Er-doped silica thin layers.

IV. CONCLUSIONS

We experimentally demonstrate that sandwiching an Er-doped SiO_2 thin film between two high-refractive-index layers can strongly enhance the radiative decay rate with negligible losses. For a 5-nm-thick emitting layer, a 20-fold shortening of the Er^{3+} lifetime is experimentally measured, with a quantum efficiency of about 90%. Furthermore, the comparison of the experimental findings with the CDO model shows almost perfect agreement between theory and experiment, also confirming the mixed ED and MD nature (with nearly equal contributions) of the Er^{3+} $^4I_{13/2} \rightarrow$ $^4I_{15/2}$ radiative transition. By means of time-integrated PL measurements, we point out that most of the emitted radiation is coupled to guided or propagating modes in silicon and just a small fraction is able to couple out directly to the far field. Nevertheless, acting on the geometry of the nanoslot, an increase of the far-field efficiency by roughly one order of magnitude can be obtained. This is verified in an array of pillarlike nanostructures that exhibit almost the same enhancement in the decay rate of the planar geometry but with a much better outcoupling of the emission in the far field.

ACKNOWLEDGMENTS

[1] E. M. Purcell, H. C. Torrey, and R. V. Pound, Resonance absorption by nuclear magnetic moments in a solid, Phys. Rev. **69**, 37 (1946).

[2] M. Fox, *Quantum Optics: An Introduction* (OUP, Oxford, 2006), Vol. 15.

[3] K. Drexhage, Influence of a dielectric interface on fluorescence decay time, J. Lumin. **1**, 693 (1970).

[4] M. De Dood, L. Slooff, A. Polman, A. Moroz, and A. Van Blaaderen, Local optical density of states in SiO_2 spherical microcavities: Theory and experiment, Phys. Rev. A **64**, 033807 (2001).

[5] D. Li, S. Karaveli, S. Cueff, W. Li, and R. Zia, Probing the Combined Electromagnetic Local Density of Optical States with Quantum Emitters Supporting Strong Electric and Magnetic Transitions, Phys. Rev. Lett. **121**, 227403 (2018).

[6] N. Michieli, B. Kalinic, C. Scian, T. Cesca, and G. Mattei, Emission rate modification and quantum efficiency enhancement of Er^{3+} emitters by near-field coupling with nanohole arrays, ACS Photonics **5**, 2189 (2018).

[7] S. Mignuzzi, S. Vezzoli, S. A. Horsley, W. L. Barnes, S. A. Maier, and R. Sapienza, Nanoscale design of the local density of optical states, Nano Lett. **19**, 1613 (2019).

[8] V. Giannini, A. I. Fernández-Domínguez, S. C. Heck, and S. A. Maier, Plasmonic nanoantennas: Fundamentals and their use in controlling the radiative properties of nanoemitters, Chem. Rev. **111**, 3888 (2011).

[9] G. M. Akselrod, C. Argyropoulos, T. B. Hoang, C. Ciracì, C. Fang, J. Huang, D. R. Smith, and M. H. Mikkelsen, Probing the mechanisms of large Purcell enhancement in plasmonic nanoantennas, Nat. Photonics **8**, 835 (2014).

[10] L. Rogobete, F. Kaminski, M. Agio, and V. Sandoghdar, Design of plasmonic nanoantennae for enhancing spontaneous emission, Opt. Lett. **32**, 1623 (2007).

[11] E. J. R. Vesseur, F. J. G. de Abajo, and A. Polman, Broadband Purcell enhancement in plasmonic ring cavities, Phys. Rev. B **82**, 165419 (2010).

[12] C. Maurizio, T. Cesca, G. Perotto, B. Kalinic, N. Michieli, C. Scian, Y. Joly, G. Battaglin, P. Mazzoldi, and G. Mattei, Core–shell-like Au sub-nanometer clusters in Er-implanted silica, Nanoscale **7**, 8968 (2015).

[13] A. Rose, T. B. Hoang, F. McGuire, J. J. Mock, C. Ciracì, D. R. Smith, and M. H. Mikkelsen, Control of radiative processes using tunable plasmonic nanopatch antennas, Nano Lett. **14**, 4797 (2014).

[14] A. F. Koenderink, Single-photon nanoantennas, ACS Photonics **4**, 710 (2017).

[15] B. Kalinic, T. Cesca, C. Scian, N. Michieli, I. G. Balasa, E. Trave, and G. Mattei, Emission efficiency enhancement of Er^{3+} ions in silica by near-field coupling with plasmonic and pre-plasmonic nanostructures, Phys. Stat. Solidi (a) **215**, 1700437 (2018).

[16] T. Cesca, N. Michieli, B. Kalinic, I. G. Balasa, R. Rangel-Rojo, J. A. Reyes-Esqueda, and G. Mattei, Bidimensional ordered plasmonic nanoarrays for nonlinear optics, nanophotonics and biosensing applications, Mater. Sci. Semicond. Process. **92**, 2 (2019).

[17] P. Anger, P. Bharadwaj, and L. Novotny, Enhancement and Quenching of Single-Molecule Fluorescence, Phys. Rev. Lett. **96**, 113002 (2006).

[18] S. A. Maier, *Plasmonics: Fundamentals and Applications* (Springer Science & Business Media, New York, 2007).

[19] P. Albella, R. Alcaraz de la Osa, F. Moreno, and S. A. Maier, Electric and magnetic field enhancement with ultralow heat radiation dielectric nanoantennas: Considerations for surface-enhanced spectroscopies, ACS Photonics **1**, 524 (2014).

[20] A. I. Kuznetsov, A. E. Miroshnichenko, M. L. Brongersma, Y. S. Kivshar, and B. Luk'yanchuk, Optically resonant dielectric nanostructures, Science **354**, aag2472 (2016).

[21] R. M. Bakker, D. Permyakov, Y. F. Yu, D. Markovich, R. Paniagua-Domínguez, L. Gonzaga, A. Samusev, Y. Kivshar, B. Luk'yanchuk, and A. I. Kuznetsov, Magnetic

and electric hotspots with silicon nanodimers, Nano Lett. **15**, 2137 (2015).

[22] I. Staude, A. E. Miroshnichenko, M. Decker, N. T. Fofang, S. Liu, E. Gonzales, J. Dominguez, T. S. Luk, D. N. Neshev, I. Brener *et al.*, Tailoring directional scattering through magnetic and electric resonances in subwavelength silicon nanodisks, ACS Nano **7**, 7824 (2013).

[23] S. Jahani and Z. Jacob, All-dielectric metamaterials, Nat. Nanotechnol. **11**, 23 (2016).

[24] A. Vaskin, J. Bohn, K. E. Chong, T. Bucher, M. Zilk, D.-Y. Choi, D. N. Neshev, Y. S. Kivshar, T. Pertsch, and I. Staude, Directional and spectral shaping of light emission with Mie-resonant silicon nanoantenna arrays, ACS Photonics **5**, 1359 (2018).

[25] J. Lu, S. Boyd, and J. Vučković, Inverse design of a three-dimensional nanophotonic resonator, Opt. Express **19**, 10563 (2011).

[26] T. Feichtner, S. Christiansen, and B. Hecht, Mode Matching for Optical Antennas, Phys. Rev. Lett. **119**, 217401 (2017).

[27] J. Cambiasso, G. Grinblat, Y. Li, A. Rakovich, E. Cortés, and S. A. Maier, Bridging the gap between dielectric nanophotonics and the visible regime with effectively loss-less gallium phosphide antennas, Nano Lett. **17**, 1219 (2017).

[28] A. Dibos, M. Raha, C. Phenicie, and J. D. Thompson, Atomic Source of Single Photons in the Telecom Band, Phys. Rev. Lett. **120**, 243601 (2018).

[29] L. Sortino, P. Zotev, S. Mignuzzi, J. Cambiasso, D. Schmidt, A. Genco, M. Aßmann, M. Bayer, S. Maier, R. Sapienza *et al.*, Enhanced light-matter interaction in an atomically thin semiconductor coupled with dielectric nano-antennas, Nat. Commun. **10**, 1 (2019).

[30] F. Priolo, T. Gregorkiewicz, M. Galli, and T. F. Krauss, Silicon nanostructures for photonics and photovoltaics, Nat. Nanotechnol. **9**, 19 (2014).

[31] C. Zhang, Y. Xu, J. Liu, J. Li, J. Xiang, H. Li, J. Li, Q. Dai, S. Lan, and A. E. Miroshnichenko, Lighting up silicon nanoparticles with Mie resonances, Nat. Commun. **9**, 1 (2018).

[32] Y. C. Jun, R. M. Briggs, H. A. Atwater, and M. L. Brongersma, Broadband enhancement of light emission in silicon slot waveguides, Opt. Express **17**, 7479 (2009).

[33] C. Creatore, L. C. Andreani, M. Miritello, R. Lo Savio, and F. Priolo, Modification of erbium radiative lifetime in planar silicon slot waveguides, Appl. Phys. Lett. **94**, 103112 (2009).

[34] C. R. Giles and E. Desurvire, Modeling erbium-doped fiber amplifiers, J. Lightwave Technol. **9**, 271 (1991).

[35] A. Polman, Erbium implanted thin film photonic materials, J. Appl. Phys. **82**, 1 (1997).

[36] A. Kenyon, Erbium in silicon, Semicond. Sci. Technol. **20**, R65 (2005).

[37] E. Snoeks, P. Kik, and A. Polman, Concentration quenching in erbium implanted alkali silicate glasses, Opt. Mater. **5**, 159 (1996).

[38] S. Coffa, G. Franzo, F. Priolo, A. Polman, and R. Serna, Temperature dependence and quenching processes of the intra-4*f* luminescence of Er in crystalline Si, Phys. Rev. B **49**, 16313 (1994).

[39] E. Trave, M. Back, E. Cattaruzza, F. Gonella, F. Enrichi, T. Cesca, B. Kalinic, C. Scian, V. Bello, C. Maurizio

et al., Control of silver clustering for broadband Er^{3+} luminescence sensitization in Er and Ag co-implanted silica, J. Lumin. **197**, 104 (2018).

[40] J. Rönn, W. Zhang, A. Autere, X. Leroux, L. Pakarinen, C. Alonso-Ramos, A. Säynätjoki, H. Lipsanen, L. Vivien, E. Cassan *et al.*, Ultra-high on-chip optical gain in erbium-based hybrid slot waveguides, Nat. Commun. **10**, 432 (2019).

[41] Z. Chen, X. Wang, F. Zhang, S. Noda, K. Saito, T. Tanaka, M. Nishio, M. Arita, and Q. Guo, Observation of low voltage driven green emission from erbium doped Ga_2O_3 light-emitting devices, Appl. Phys. Lett. **109**, 022107 (2016).

[42] S. Zhu, L. Shi, B. Xiao, X. Zhang, and X. Fan, All-optical tunable microlaser based on an ultrahigh-*Q* erbium-doped hybrid microbottle cavity, ACS Photonics **5**, 3794 (2018).

[43] N. Li, D. Vermeulen, Z. Su, E. S. Magden, M. Xin, N. Singh, A. Ruocco, J. Notaros, C. V. Poulton, E. Timurdogan *et al.*, Monolithically integrated erbium-doped tunable laser on a CMOS-compatible silicon photonics platform, Opt. Express **26**, 16200 (2018).

[44] A. Alizadehkhaledi, A. Frencken, F. C. van Veggel, and R. Gordon, Isolating nanocrystals with an individual erbium emitter: A route to a stable single-photon source at 1550 nm wavelength, Nano Lett. **20**, 1018 (2019).

[45] D. Li, M. Jiang, S. Cueff, C. M. Dodson, S. Karaveli, and R. Zia, Quantifying and controlling the magnetic dipole contribution to 1.5-μm light emission in erbium-doped yttrium oxide, Phys. Rev. B **89**, 161409 (2014).

[46] R. Chance, A. Prock, and R. Silbey, Molecular fluorescence and energy transfer near interfaces, Adv. Chem. Phys **37**, 1 (1978).10.1002/9780470142561.ch1

[47] L. Slooff, M. De Dood, A. Van Blaaderen, and A. Polman, Effects of heat treatment and concentration on the luminescence properties of erbium-doped silica sol-gel films, J. Non Cryst. Solids **296**, 158 (2001).

[48] T. Cesca, C. Maurizio, B. Kalinic, G. Perotto, P. Mazzoldi, E. Trave, G. Battaglin, and G. Mattei, Implantation damage effects on the Er^{3+} luminescence in silica, Opt. Express **20**, 16639 (2012).

[49] E. D. Palik, *Handbook of Optical Constants of Solids* (Academic Press, Orlando, 1998), Vol. 3.

[50] C. Wenshan and V. Shalaev, *Optical Metamaterials: Fundamentals and Applications* (Springer-Verlag, New York, 2010).

[51] Y. Xu, R. Huang, and G. Rigby, A study of sputter deposited silicon films, J. Electron. Mater. **21**, 373 (1992).

[52] W. J. Miniscalco, Erbium-doped glasses for fiber amplifiers at 1500 nm, J. Lightwave Technol. **9**, 234 (1991).

[53] T. Cesca, B. Kalinic, C. Maurizio, C. Scian, G. Battaglin, P. Mazzoldi, and G. Mattei, Interatomic coupling of Au molecular clusters and Er^{3+} ions in silica, ACS Photonics **2**, 96 (2014).

[54] B. C. Sturmberg, K. B. Dossou, F. J. Lawrence, C. G. Poulton, R. C. McPhedran, C. M. De Sterke, and L. C. Botten, EMUstack: An open source route to insightful electromagnetic computation via the Bloch mode scattering matrix method, Comput. Phys. Commun. **202**, 276 (2016).

[55] See the Supplemental Material at http://link.aps.org/supplemental/10.1103/PhysRevApplied.14.014086, which includes Refs. [68] and [69], for additional information

about the CDO model, the measurement of the Er^{3+} radiative decay rate in SiO$_2$, and the simulated electric fields.

[56] J. Bao, N. Yu, F. Capasso, T. Mates, M. Troccoli, and A. Belyanin, Controlled modification of erbium lifetime in silicon dioxide with metallic overlayers, Appl. Phys. Lett. **91,** 131103 (2007).

[57] B. Kalinic, T. Cesca, N. Michieli, C. Scian, G. Battaglin, P. Mazzoldi, and G. Mattei, Controlling the emission rate of Er^{3+} ions by dielectric coupling with thin films, J. Phys. Chem. C **119,** 6728 (2015).

[58] R. Chance, A. Prock, and R. Silbey, Comments on the classical theory of energy transfer. II. Extension to higher multipoles and anisotropic media, J. Chem. Phys. **65,** 2527 (1976).

[59] S. Karaveli and R. Zia, Strong enhancement of magnetic dipole emission in a multilevel electronic system, Opt. Lett. **35,** 3318 (2010).

[60] W. Barnes, Fluorescence near interfaces: The role of photonic mode density, J. Mod. Opt. **45,** 661 (1998).

[61] J. Kalkman, L. Kuipers, A. Polman, and H. Gersen, Coupling of Er ions to surface plasmons on Ag, Appl. Phys. Lett. **86,** 041113 (2005).

[62] R. Amos and W. Barnes, Modification of the spontaneous emission rate of Eu^{3+} ions close to a thin metal mirror, Phys. Rev. B **55,** 7249 (1997).

[63] A. Polman and F. C. van Veggel, Broadband sensitizers for erbium-doped planar optical amplifiers, JOSA B **21,** 871 (2004).

[64] M. Galli, D. Gerace, A. Politi, M. Liscidini, M. Patrini, L. C. Andreani, A. Canino, M. Miritello, R. L. Savio, A. Irrera *et al.*, Direct evidence of light confinement and emission enhancement in active silicon-on-insulator slot waveguides, Appl. Phys. Lett. **89,** 241114 (2006).

[65] E. Snoeks, A. Lagendijk, and A. Polman, Measuring and Modifying the Spontaneous Emission Rate of Erbium near an Interface, Phys. Rev. Lett. **74,** 2459 (1995).

[66] G. Van den Hoven, E. Snoeks, A. Polman, J. Van Uffelen, Y. Oei, and M. Smit, Photoluminescence characterization of Er-implanted Al$_2$O$_3$ films, Appl. Phys. Lett. **62,** 3065 (1993).

[67] M. Galli, A. Politi, M. Belotti, D. Gerace, M. Liscidini, M. Patrini, L. Andreani, M. Miritello, A. Irrera, F. Priolo *et al.*, Strong enhancement of Er^{3+} emission at room temperature in silicon-on-insulator photonic crystal waveguides, Appl. Phys. Lett. **88,** 251114 (2006).

[68] R. Chance, A. Prock, and R. Silbey, Comments on the classical theory of energy transfer, J. Chem. Phys. **62,** 2245 (1975).

[69] T. H. Taminiau, S. Karaveli, N. F. Van Hulst, and R. Zia, Quantifying the magnetic nature of light emission, Nat. Commun. **3,** 979 (2012).